Applied Catalysis B: Environmental 251 (2019) 295–304

Contents lists available at ScienceDirect

Applied Catalysis B: Environmental

journal homepage: www.elsevier.com/locate/apcatb

Surface properties enhanced Mn_xAlO oxide catalysts derived from Mn_xAl layered double hydroxides for acetone catalytic oxidation at low temperature

Yonggang Sun[a,b], Xin Zhang[a,*], Na Li[a,b], Xin Xing[a,b], Hongling Yang[a,b], Fenglian Zhang[a,b], Jie Cheng[a], Zhongshen Zhang[a], Zhengping Hao[b,*]

[a] National Engineering Laboratory for VOCs Pollution Control Material & Technology, University of Chinese Academy of Sciences, Beijing, 101408, PR China
[b] Research Center for Eco-Environmental Sciences, Chinese Academy of Sciences, Beijing, 100085, PR China

ARTICLE INFO

Keywords:
Surface properties
Acetone
Layered double hydroxides
Catalytic activity
Reaction mechanism

ABSTRACT

Mn_xAlO mixed oxide catalysts derived from Mn_xAl-LDHs were prepared and tested for acetone catalytic oxidation. Detailed results indicated that the surface intrinsic and formed oxygen vacancies can induce the Mn-O bond of structural unit [MnO_6] weakened. Subsequently, it can improve the redox properties of catalysts, and enhance the capacity of gaseous oxygen species dissociation and adsorption. Among them, Mn_3AlO catalyst displayed the best catalytic performance for acetone oxidation (T_{90} = 164 °C) with the production of low amount of byproduct (< 5 ppm) and high CO_2 yield (> 99%) producted. Additionally, the Mn_3AlO catalyst can proceed consecutively for 12 h reaction without notable deactivation. Furthermore, *in situ* DRIFT and theoretical calculations methods was adopted to explore the reaction mechanism. And $\eta1(O)_{(ads)}$ (adsorption mode of acetone), $CH_2=C(CH_3)=O_{(ads)}$, O*, CH_3CHO*, CH_2O* and $COO_{(ads)}$ were considered as the main intermediate species and/or transient state during the reaction process. It was revealed that the acetone and oxygen molecules were activated by the dehydrogenation (α-H abstraction) and dissociation process over Mn_3AlO catalyst, respectively, and then the intermediate specie, $CH_2{=}C(CH_3){=}O$ and O*, were produced, which was followed by the breaking of −C−C− bonds to produce the CH_3CHO* and CH_2O* species. Finally, these species were attacked by dissociated oxygen (O*) and therefore further dehydrogenation occurred, form H_2O and CO_2 via the COO− adsorbed species. Particularly, −C−C− bond breaking was the main rate determining step for acetone oxidation.

1. Introduction

Oxygenated volatile organic compounds (OVOCs), mainly ketone compounds, are ubiquitous and abundant components in the environment that have received special attention due to their high reactivity [1–3]. OVOCs can greatly influence human health and the environmental quality through the formation of ozone, secondary organic aerosols, and ground level smog [4–6]. Among them, acetone is regarded as a typical OVOC, which is extensively used in the packaging and printing industry, manufacture of plastics, paint thinners, and adhesives [7,8]. Therefore, it is extremely necessary and urgent to solve the pollution of this kind VOCs as well as the high standards of environmental protection concept.

As is known, catalytic oxidation is considered as one of the most promising and effective techniques for the removal of VOCs. Particularly, transition metal oxide based catalysts are economic favorites and resistant to poisoning. Hence, it is considered a promising catalyst for the elimination of OVOCs. However, the further application of metal oxide based catalytic oxidation acetone suffers from the disadvantage of relatively poor catalytic activity (T_{90} > 200 °C) associated with unsatisfactory stability (coking effect) [9–13]. Furthermore, little is known about the reaction mechanism and the catalyst deactivation for acetone oxidation. As such, it is extremely important to design efficient catalysts with excellent activity, explore and elucidate the catalytic reaction mechanism to avoid and control reaction byproducts formed.

It is known that layered double hydroxides (LDHs) are a class of lamellar compounds that has attracted an increasing interest in various catalytic reactions. The general formula that specifies this class of materials is $[M^{2+}_{(1-x)}M^{3+}_{x}(OH)_2]^{x+}[A_{x/n}{}^{n-}]\cdot mH_2O$, where x represents the fraction of the M^{3+} cation. The difference values of M^{2+}/M^{3+} in brucite-like layers can result in the different distributional local

* Corresponding authors.
E-mail addresses: zhang@ucas.ac.cn (X. Zhang), zpinghao@rcees.ac.cn (Z. Hao).

https://doi.org/10.1016/j.apcatb.2019.03.035
Received 18 February 2019; Received in revised form 6 March 2019; Accepted 12 March 2019
Available online 31 March 2019
0926-3373/ © 2019 Elsevier B.V. All rights reserved.

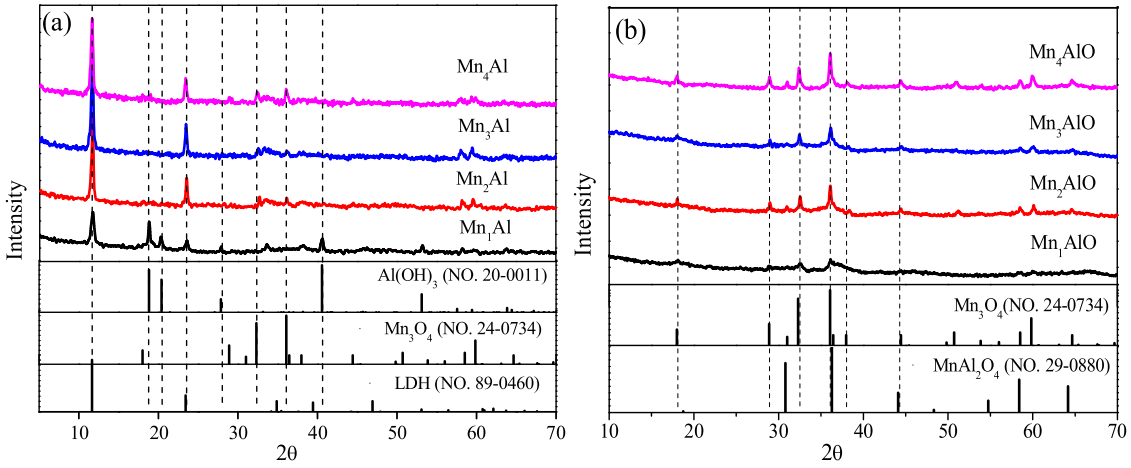

Fig. 1. XRD patterns of Mn_xAl-LDH and Mn_xAlO samples.

environmental of the metal cation [14–16]. Additionally, the uniformity and dispersity of metal cations in the octahedral sites can be adjusted and controlled on the atomic level, which is closely related to the catalytic performance. Briefly, LDH-derived mixed oxides possess several pivotal properties such as easy preparation, high surface area, and tunable composition and structure. Therefore, it has attracted particular interest for VOCs catalytic oxidation, such as aromatics [17–19], olefins and saturated alkanes oxidation [20]. On the other hand, the Mn element is widely applied as an active species for VOCs removal due to multiple coordination numbers, oxidized states, high redox potential, environmental friendliness and low cost [21–24].

Therefore, in this work, a series of Mn_xAlO catalysts derived from Mn_xAl-LDHs were prepared, and the catalytic characteristics were examined in detail by various techniques and methods. The different influence factors of the prepared catalysts were investigated for the catalytic oxidation of acetone. The relationship between the surface properties and catalytic performance was defined. Moreover, the catalytic mechanism, reaction pathways and rate-determining step were tentatively proposed based on reaction detection, *in situ* DRIFT and first-principle theoretical calculations.

2. Material and methods

2.1. Synthesis of Mn_xAlO catalysts

The co-precipitation method was used to prepare of Mn_xAl-LDHs samples with different Mn/Al molar ratio. Briefly, the mixed solution of Na_2CO_3-NaOH and mixed Mn-Al nitrate solution (molar ratio of Mn/Al = 1.0, 2.0, 3.0, and 4.0) were introduced drop-wise simultaneously to reactor under stirring and N_2 atmosphere, and maintained the pH constant (pH = 10.5). It was stirred for 3 h and then aged 12 h under N_2 atmosphere at room temperature. The resulting slurry was washed and dried at 100 °C for 24 h, it was named Mn_xAl-LDH, subsequently, the Mn_xAlO catalysts was obtained by heat Mn_xAl-LDH precursors in air at 550 °C for 2 h.

2.2. Characterization and evaluation of the catalysts

The catalysts characterization and evaluation section was seen in supplementary material.

2.3. Theoretical calculation

First-principle calculations were carried with the all-electron code Fritz-Haber Institute *ab* initio molecules simulations package (FHI-aims) [25]. The exchange-correlation potentials were treated by the generalized gradient approximation (GGA) parametrized by Perdew, Burke, and Ernzerholf (PBE) [26]. Periodic (001) Mn_3O_4 surface slab was proposed to simulate the adsorption process, and the vacuum layer between neighboring models was at least 20 Å to reduce the electrostatic interactions between them. The Brillion zone was sampled by an appropriate Monkhorst-Pack grid with a density of at least 0.03 $Å^{-1}$ [27]. The bottom two layers were fixed at bulk lattice sites, the top three ones and all adsorbates were relaxed until the charge density and the total energy were below of 10^{-4} eV/$Å^3$ and 10^{-5} eV, respectively. Spin polarization calculation was employed for the identifications of different chemical valence of Mn. To account for the vdW interactions between molecules and solid surfaces, the vdW^{surf} approach was performed using the Tkatchenko and Scheffler scheme [28].

The DFT adsorption energy of the acetone and inorganic molecule, which described the stability of the system, were calculated by

$$\Delta E_{ads} = E_{system} - E_{substrate} - E_{adsorbate}$$

Where E_{system} was the total energy for an adsorbate on Mn_3O_4 (001) substrate, $E_{substrate}$ was the total energy for the Mn_3O_4 substrate without adsorbates, and $E_{adsorbate}$ was the total energy of an isolated adsorbate as determined from the calculations. Furthermore, transition states for several possible pathways of the acetone oxidation on Mn_3O_4 surfaces were obtained using the nudged elastic band (NEB) method [29].

3. Results and discussions

3.1. Structural and texture characteristic

The XRD patterns of the Mn_xAl-LDH precursors are presented in Fig. 1**a**. The patterns present extremely different characteristics with the increase of Mn/Al ratio. In the case of Mn_1Al-LDH, the diffraction profile reveals the coexistence of LDH (JCPDS-NO.89-0460) structure and $Al(OH)_3$ (JCPDS-NO.20-0011), which can be assigned to excess aluminum in the initial Mn-Al solution. Correspondingly, the peaks centered at 2θ = 11.6° and 23.4° are related to MnAl- LDH, while the peaks near 2θ = 18.8°, 20.4°, 40.5°, and 53.1° are the typical diffractions of $Al(OH)_3$. Upon increasing the Mn/Al ratio from 2 and 3, the pronounced peaks at 11.6°, 23.4°, 34.5° and 39.2° reveal only the presence of MnAl-LDHs. Subsequently, for the Mn_4Al-LDH catalyst, the new peak at 36.0° indicates the continued existence of Mn_3O_4 (JCPDS-NO.24-0734). In addition, the textural parameters, adsorption-desorption isotherms, pore distributions and chemical composition of the Mn_xAlO samples are listed in Table 1 and **Figure S1.** The Mn_xAlO samples possess a typical type IV isotherm with type-H3 hysteresis loops. The hysteresis loops indicate the presence of mesopores, similar structural parameters of average pores diameter (~6 nm) and pore volume (~0.2 $cm^3\,g^{-1}$) were observed. The average particle size (~25 nm)

Table 1
Physico-chemical characteristics and compositions of Mn_xAlO catalysts.

Sample	Textural parameters				Chemical composition[e]			Normalized peak area[f]
	S_{BET}[a]	D_{pd}[b]	V_{pv}[c]	G_{gs}[d]	Mn	Al	Mole ratio Mn/Al	
Mn_1AlO	145.9	6.7	0.40	26.2	23.0	8.8	1.29	1.9
Mn_2AlO	128.2	6.0	0.30	25.5	37.6	8.9	2.07	2.1
Mn_3AlO	115.7	6.2	0.23	22.4	51.9	8.2	3.10	2.3
Mn_4AlO	81.5	7.7	0.26	25.3	55.4	6.7	4.04	1.0

[a] S_{BET}: refers to specific surface area ($m^2\,g^{-1}$).
[b] D_{pd}: refers to Pore diameter (nm).
[c] V_{pv}: refers to Pore volume ($cm^3\,g^{-1}$).
[d] G_{gs}: refers to average particle size (nm), calculated from Scherrer equation.
[e] Bulk chemical composition was measured by ICP-OES (wt%).
[f] Normalized integrated areas results for the peaks at 585 cm^{-1} over Raman spectra, the integrated areas of Mn_4AlO sample was defined as one, it was as a reference.

was analyzed by HR-TEM images (**Figure S2**). ICP-OES illustrates that the bulk chemical composition was similar to the Mn/Al molar ratio of the synthetic Mn_xAlO samples.

3.2. The chemical state of Mn species

The chemical state of the active phase plays a crucial role in the catalytic reaction. The reaction rate and reaction pathway mostly rely on the nature of the active phase. Therefore, it is important to explore the chemical state of Mn species in the prepared catalysts. The spectra of the LDH calcined at 550 °C are established in Fig. 1**b**. All the neat spectra illustrate the complete conversion of LDH to well mixed oxide. The pronounced diffraction peaks at 17.8°, 29.0°, and 36.1° are mainly attributed to the spinel-like Mn_3O_4 phase concurrent with $MnAl_2O_4$ (JCPDS-NO.29-0880) at 36.4°.

Raman vibrational spectrum can directly probe the structure and bonding of a transition-metal oxide complex, therefore, it can be used to discriminate different structures. Fig. 2 shows representative Raman scattering spectra of the Mn_xAlO catalyst. The spectra was dominated by only a broad peak, which can be further divided into two peaks centered at 650 cm^{-1} and 585 cm^{-1}, respectively. Particularly, the peaks at 650 cm^{-1} can be recognized as the v_2 (Mn−O) symmetric stretching vibration of the [MnO_6] group in a Mn_3O_4 structure [30].

Additionally, XPS measurement was further conducted to characterize the chemical state of the Mn species in the near-surface region. The Mn 2p3/2 and Mn 3 s XPS spectra of these catalysts are provided in Fig. 3**a-c**. It can be seen that the peaks corresponding to Mn the 2p3/2 spectra can be broken down into three components related to Mn^{4+} at 641.9 eV, Mn^{3+} at 642.8 eV, and the satellite of Mn^{3+} species at 644.1 eV, respectively. Subsequently, a quantitative analysis of the molar ratios and contents of surface Mn^{4+}/Mn^{3+} and Mn^{4+} are summarized in Table 2. Among them, the Mn_3AlO catalyst possesses the most Mn^{4+} and highest molar ratio of Mn^{4+}/Mn^{3+} (0.68) on the surface. More surface Mn^{4+} ions may increase the oxygen vacancies of an oxide material, which is beneficial to the adsorption, activation and migration of oxygen in the gas phase [31].

Upon the above results, it demonstrates that Mn was mainly existed in the form of Mn_3O_4. Notably, the Mn_3AlO catalyst possesses the highest of surface Mn^{4+} content.

3.3. Surface oxygen properties

The capability of oxygen species transmission and migration was expressed by O_2-TPD-MS. The more accurate qualitative analysis of MS signaling was adopted. As shown in the O_2-MS (m/z = 32) profiles of Fig. 4a, the peak at high temperature (570 °C) was assigned to the desorption of O^- and O^{2-} species that are probably from oxygen adsorbed on the oxygen vacancy and labile lattice oxygen of metal oxides [32,33]. The peak above 700 °C was due to the evolution of bulk lattice oxygen [34]. The evolution of O_2 was estimated by integrating the area of the O_2-MS (m/z = 32) curves, and the results are listed in **Table S1**. It is worth mentioning that Mn_3AlO possesses the highest O_2 desorption capacity, illustrating that the Mn_3AlO catalyst contains abundant oxygen vacancies and intrinsic loosely bound active oxygen species.

The O 1 s XPS profile also confirms the coexistence of surface chemical oxygen adsorbed on the oxygen vacancy and lattice oxygen. As shown in Fig. 3d, the first peak at 529.3 eV was attributed to lattice O (O^{2-}) in a coordinately saturated environment, the second (530.9 eV) was the characteristic of the surface adsorbed O (O_2^{2-}, O_2- or O-) and oxygen defects in the unsaturated coordination modes. Among them, the Mn_3AlO catalyst had a greater amount of electrophilic, surface adsorbed O (O_{ads}/O_{lat} = 1.44), which is in good agreement with the O_2-MS results. Therefore, the enhanced surface oxygen properties can be enormously beneficial for the total oxidation of acetone.

Besides, the oxygen vacancy concentration can be indirectly calculated by the Raman peak at 585 cm^{-1} [35,36]. The corresponding normalized results are shown in Fig. 2**a** and Table 1. The oxygen vacancy concentration follows the order Mn_3AlO > Mn_2AlO > Mn_4AlO > Mn_1AlO, significantly, as shown in Fig. 2b, the change in the Mn-O bond force constant of the Mn_xAlO sample was also observed. According to Hooke's law [37], the Mn-O bond force constant (k) was caculated as shown in follows.

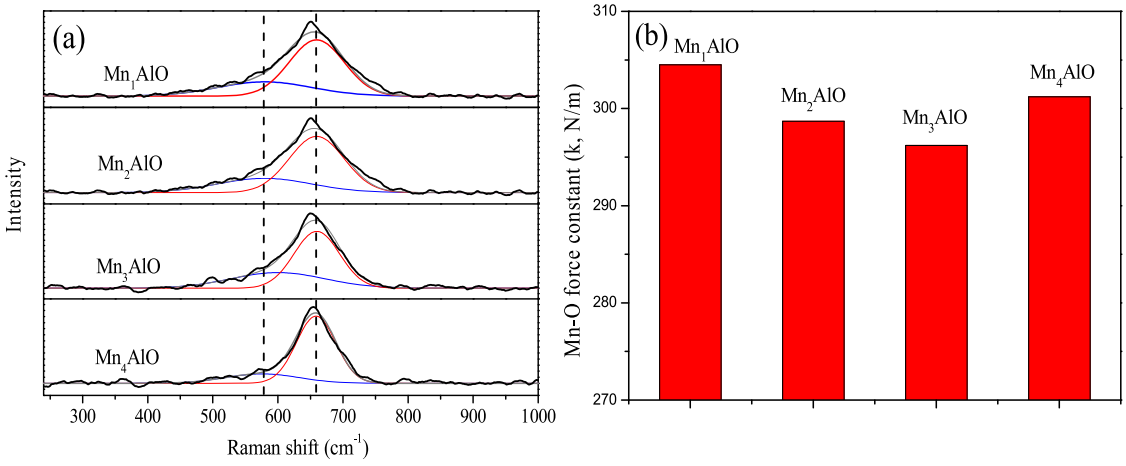

Fig. 2. Raman spectra and Mn-O bond force constant of Mn_xAlO catalysts for different Mn/Al molar ratio.

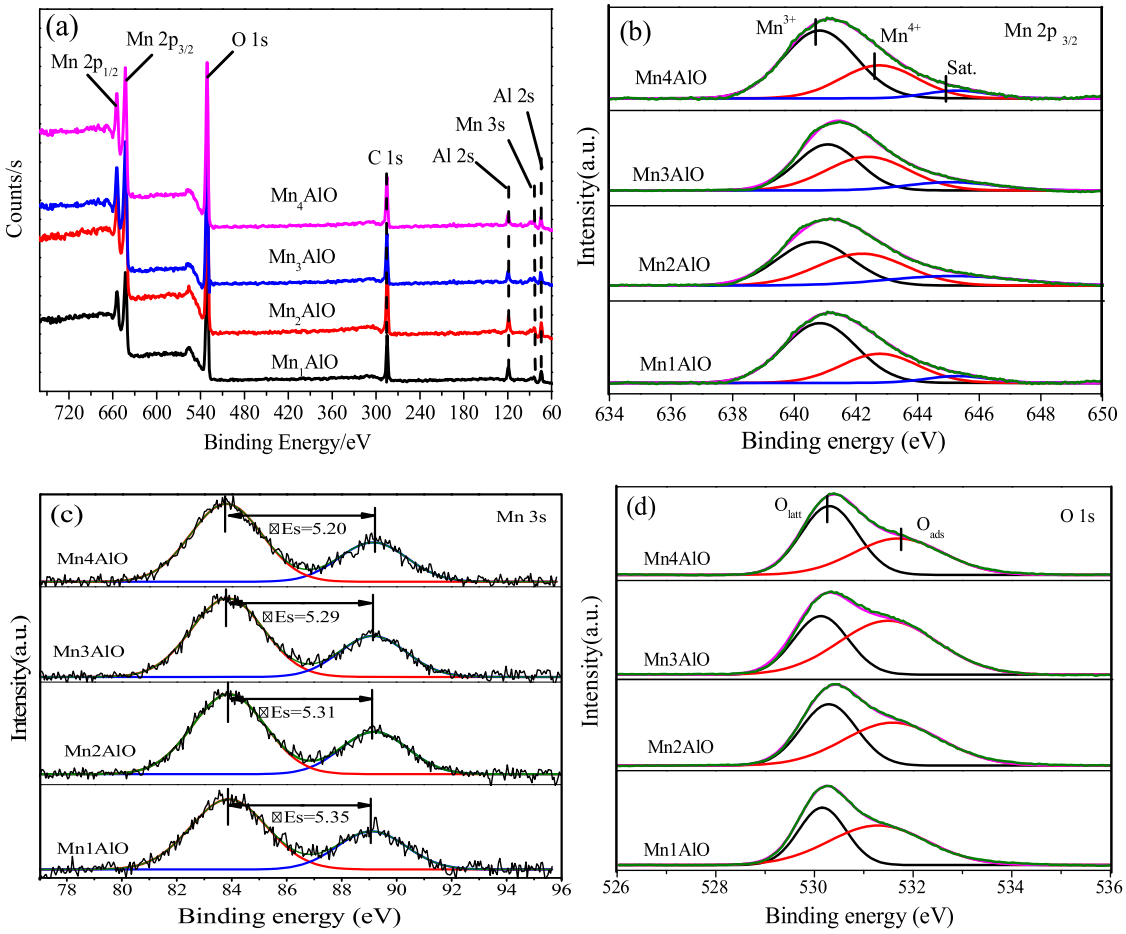

Fig. 3. XPS spectra in the full spectrum, Mn2p, Mn 3 s, and O1 s region of Mn_xAlO catalysts.

Table 2
Summary of the results of XPS analysis.

		Mn_1AlO	Mn_2AlO	Mn_3AlO	Mn_4AlO
Surface Atomic%	Mn	14.51	17.07	19.32	18.71
	Al	25.50	22.92	19.50	22.83
	O	59.99	60.01	61.18	58.46
Mn2p3/2	Mn^{3+}/mol.%	68.14	61.03	58.94	73.44
	Mn^{4+}/mol.%	31.86	38.97	41.06	26.56
	Mn^{4+}/Mn^{3+}	0.47	0.64	0.68	0.36
O1 s	O_{latt}/mol.%	42.17	44.13	40.97	53.91
	O_{ads}/mol.%	57.83	55.87	59.03	46.09
	O_{ads}/O_{latt}	1.37	1.27	1.44	0.85

$$\sigma = \frac{1}{2\pi c}\sqrt{\frac{k}{\mu}}$$

Where σ is the Raman shift (cm^{-1}) approximately 650 cm^{-1} for this model, c is the velocity of light, and μ is the effective mass of the Mn—O bond.

The detailed results show that the Mn_3AlO sample displayed a minimum Mn-O force constant (k). It is well known that the weakening of Mn—O bonds can lead to the increase in oxygen species mobility and redox properties. Therefore, it likely the catalytic performance for Mn_xAlO catalyst can be improved greatly due to the abundant presence of oxygen vacancies and a weakened Mn—O bond.

3.4. Redox properties

The reducibility of the Mn active phase, an important factor determining the activity in oxidation reactions [38], was investigated by the H_2-TPR. As shown in Fig. 4, the neat curve can be classified into two main peaks. The low temperature peak (I, T < 350 °C) could be attributed to reduction of MnO_x to Mn_2O_3/Mn_3O_4 and the high temperature reduction peak (II, T > 400 °C) is assigned to the reduction of Mn_2O_3/Mn_3O_4 to MnO. Moreover, it is important to note that the lowest reduction temperature was detected for Mn_3AlO (Fig. 4b). Meanwhile, it also displayed the more hydrogen consumption for Mn^{4+} species (0.60 mmol/g) than that observed for the other Mn_xAlO catalysts (**Table S1**). A more in-depth analysis as used to evaluate the local differences of Mn_xAlO sample reducibility. The initial H_2 consumption rate was adopted. As shown in **Figure S3** [39], the initial H_2 consumption rate decreased in the sequence of Mn_3AlO > Mn_2AlO > Mn_4AlO > Mn_1AlO, indicating that more abundant surface manganese oxide species can be in higher oxidation states, which was constant with XPS analysis.

3.5. Catalytic performances

3.5.1. Effect of reaction temperature

The catalytic activity for the total oxidation of acetone as a function of temperature is established in Fig. 5. The temperatures of 10% (T_{10}), 50% (T_{50}), and 90% (T_{90}) acetone conversion at a space velocity of 18 000 mL g^{-1} h^{-1} are summarized in **Table S1**. As shown in Fig. 5a, the catalytic activity increased with an increase in reaction temperature. Importantly, the Mn_3AlO catalyst is the most active among all these catalysts, achieving T_{90} acetone conversion at 164 °C. The high of CO_2 yield (> 99%) (Fig. 5b) and the low amount of byproduct (< 5 ppm) (Fig. 5c) was also observed. The activity was much higher than that reported in the literature **(Table S2)** [9,10]. The change in byproduct content was very consistent with the catalytic activity, oxygen vacancy concentration and reducibility. Specifically, the excellent catalytic

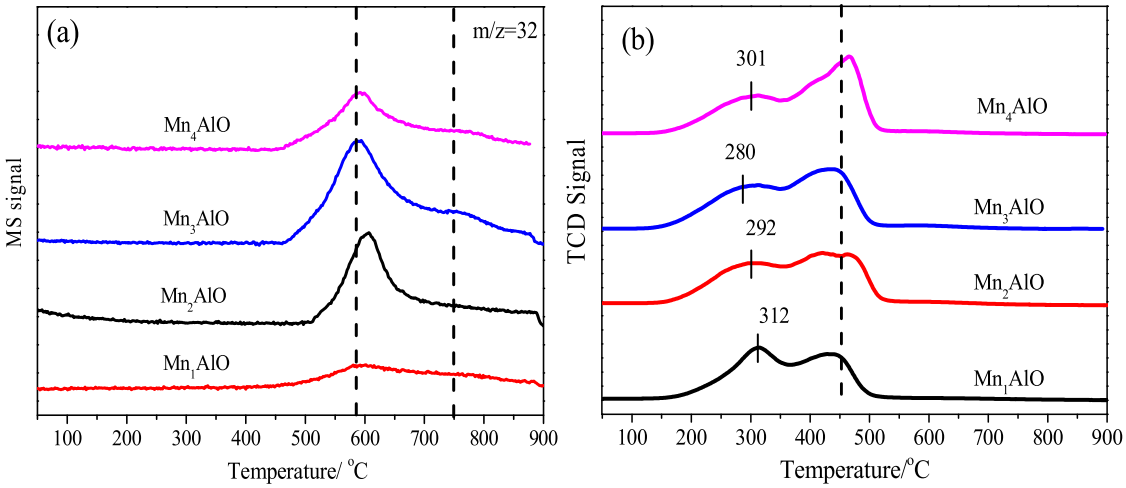

Fig. 4. O_2-MS and H_2-TPR profiles of Mn_xAlO catalysts.

performance of Mn_3AlO was due mainly to the abundant existence of surface oxygen vacancy and superior redox properties. Additionally, to better understand the catalytic performance, the activation energy E_a was also calculated. The Arrhenius plots for the oxidation of acetone are displayed in Fig. 5d, and the E_a values are listed in **Table S1.** The results indicate that lower E_a values of Mn_3AlO (36.2 kJ mol^{-1}) were obtained than that of Mn_1AlO (41 kJ mol^{-1}), Mn_2AlO (37.7 kJ mol^{-1}), and Mn_4AlO (43.4 kJ mol^{-1}), which confirm that acetone molecules could proceed with easier activation on the Mn_3AlO catalyst.

Besides, the catalyst stability and influence of acetone initial concentration and space velocity on the catalytic performance were also examined over the Mn_3AlO catalysts and listed in Fig. 5**e-g**. The results indicate that a slightly higher reaction temperature (T_{90} < 191 °C) and byproduct concentration (< 8 ppm) were required and observed for the complete conversion of acetone when the acetone concentration was increased to 500 ppm and the reaction space velocity increased from 18,000 mL g^{-1} h^{-1} to 54,000 mL g^{-1} h^{-1}, respectively. This may be caused by the shorter retention time of acetone and acetaldehyde in the catalyst bed under higher space velocity. However, the catalytic activity was still better than that of literature reports **(Table S2)** [9,13]. Additionally, Mn_3AlO maintained high stability of the acetone removal of approximately 99% without noticeable activity loss through a 12 h test.

3.5.2. Effect of water vapor

The emission of VOCs is often accompanied by water vapor. Therefore, the effect of water vapor on Mn_3AlO catalytic performance was investigated. As shown in Fig. 6**a** and **b**, the acetone conversion decreased when water vapor was introduced into system at 150 °C. Additionally, the CO_2 yield and concentration of acetaldehyde also decreased. However, a new byproduct of acetic acid was detected. When the water vapor was cut off, the acetone conversion nearly recovered, the CO_2 yield and the concentration of acetaldehyde also nearly recovered, and acetic acid was no longer detected.

To investigate the water influence mechanism, the experiments of $(CH_3)_2CO$-TPD, CO_2-TPD and H_2O-TPD were performed using Micromeritics AutoChem 2720 chemisorption. As shown in Fig. 6c, all catalysts showed only a single desorption peak in this temperature range. Compared with the maximum of the reactant and resultant desorption temperature and quantity, the H_2O molecular desorption on the Mn_3AlO catalyst was more difficult than that of CO_2 and acetone, which suggests that the H_2O desorption process may be the main factor for acetone catalytic oxidation. As a result, the vapor water adsorption test was also carried out to evaluate the endurance of the catalyst. The breakthrough curves of acetone after absorption water for 60 min and without absorption water are shown in Fig. 6**d**. Water and acetone molecules competitively adsorbed on the active sites, subsequently, the reaction pathway was changed [40].

If the postulate that water competes with acetone molecules to occupy the active sites leading the decrease of catalytic performance was viable, the water can barely influence the catalytic performance when the reaction temperature exceeds the water desorption temperature. Fortunately, this phenomenon was noted when the temperature was increased to 190 °C. As shown in Fig. 6**a and e**, the detailed results demonstrate that their absence or presence of water vapor in the system cannot effect on acetone catalytic activity at 190 °C.

3.6. Reaction mechanism

Although the catalyst presented excellent catalytic activity for acetone oxidation, however, little is known about the reaction mechanism as prepared catalyst exhibit obviously different reaction pathway. Therefore, there is an urgently need to elucidate the catalytic reaction mechanism to avoid and control the reaction byproduct formed.

3.6.1. In situ DRIFT

The reaction of acetone on the surfaces of Mn_3AlO was conducted by using *in situ* DRIFT detecting. As shown in Fig. 7a, the *in situ* spectra gradually changed with the increase of reaction time at 30 °C. The spectra were dominated by the bands at 1698 cm^{-1} corresponding to the $(CH_3)_2CO$ (ads) species. Particularly, this bonding configuration of acetone considered by the relatively electron rich carbonyl oxygen, it donates a lone pair of electrons to form a σ bond with an Mn−O site [41,42]. Importantly, a new band at 1562 cm^{-1} was gradually appeared with reaction time. According to literature [43], the new band was related to dissociatively enolate complex (CH_2=C(CH_3)=O) species [44], which was thought to derive from the transform of the η1(O) adsorption species. The bands at 1431 cm^{-1} and 1347 cm^{-1} are attributed to the carboxylate species (COO−), the band at 1369 cm^{-1} was derived from the methyl (−CH_3) vibration of acetone molecules, the band at 1237 cm^{-1} may be assigned to the carbon framework stretching vibration of adsorptive acetone. Subsequently, as shown in Fig. 7b, the band at 1698 cm^{-1} weakened, and in turn, the band at 1562 cm^{-1} was strengthened significantly with the temperature rise to 70 °C. Notably, the band at 1698 cm^{-1} almost vanished and the band at 1562 cm^{-1} governed the spectra. The bands at 1431 cm^{-1} and 1347 cm^{-1} in the 70 °C *in situ* spectra was strengthened more than that of 30 °C, indicating a more carboxylate species was produced by oxidation of the surface dissociatively enolate complex. The band at 1237 cm^{-1} was weakened due to the decrease of the η1(O) adsorption species. When the reaction temperature reached 110 °C, the η1(O) adsorption species was almost completely converted to the enolate complex species (as

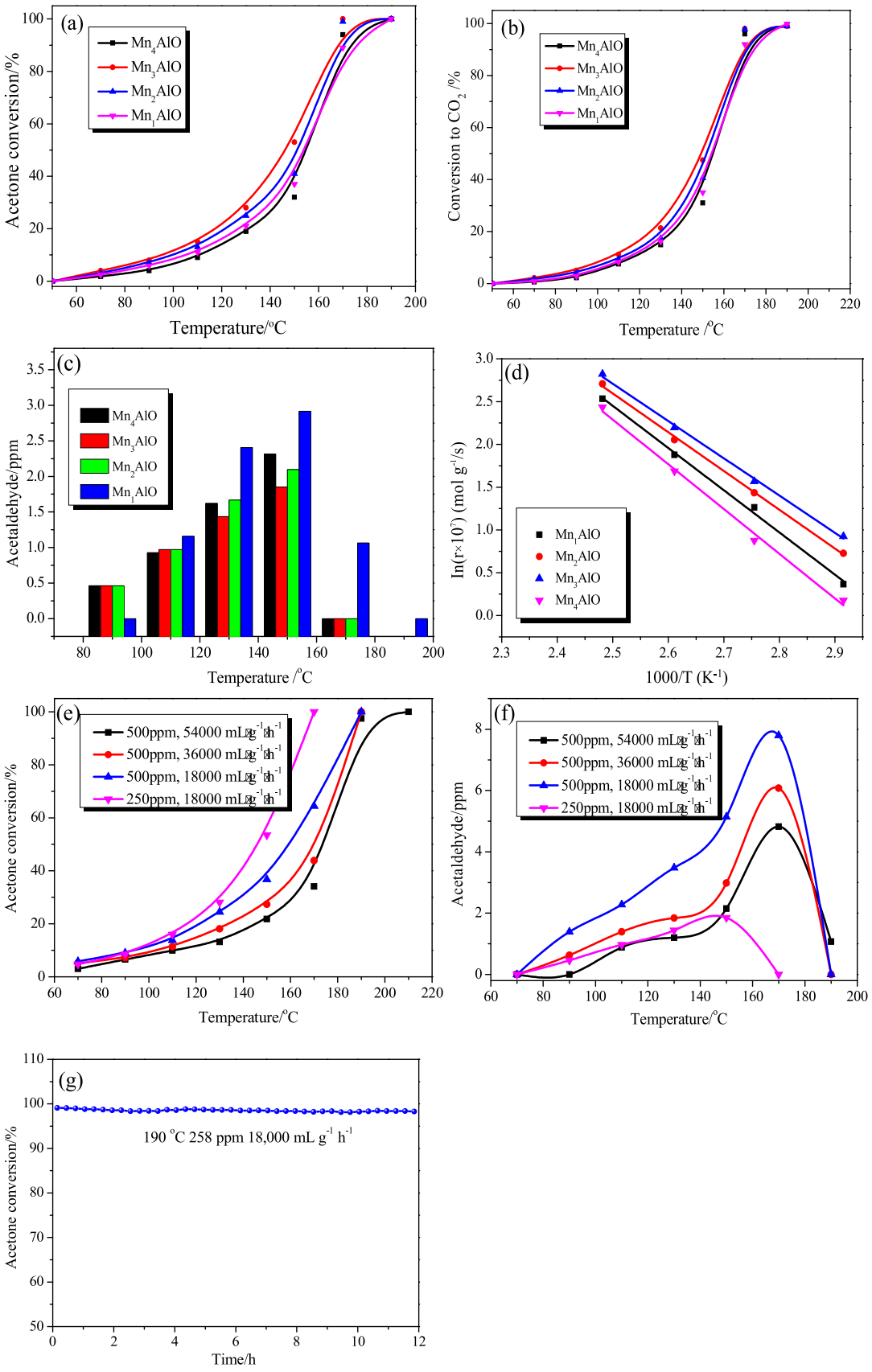

Fig. 5. The light-off curves, conversion to CO_2, byproduct concentration, Arrhenius plots for acetone catalytic oxidation at various initial concentrations and space velocity.

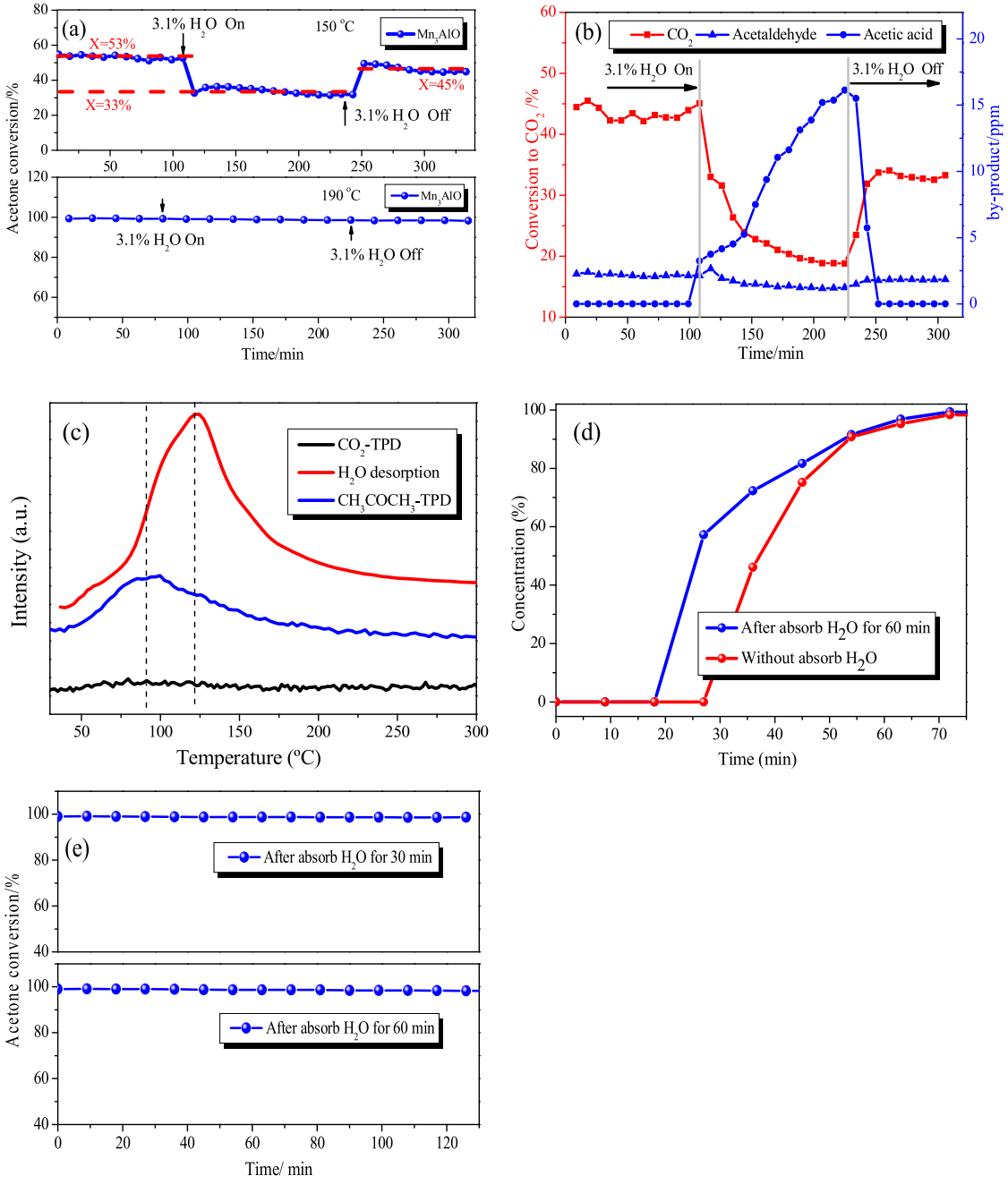

Fig. 6. Effect of water vapor on acetone catalytic oxidation at 150 °C and 190 °C for Mn_3AlO catalyst, and the CO_2-TPD, H_2O-TPD, and CH_3COCH_3-TPD profiles of the Mn_3AlO catalysts.

shown in Fig. 7c). The evolution of adsorption species is displayed in Fig. 7**d**. The detailed results show that the $(CH_3)_2CO_{(ads)}$ (1698 cm^{-1}) adsorption mode was weakened and disappeared with the temperature increased from 30 °C to 190 °C. Alternatively, the $CH_2=C(CH_3)=O_{(ads)}$ (1562 cm^{-1}) and COO- (1431 cm^{-1}, 1347 cm^{-1}) adsorption species were strengthened.

Comparing the *in situ* spectra variation with the catalytic performance, the catalytic pathway was closely related to the η1(O) adsorption species, dissociatively enolate complex ($CH_2=C(CH_3)=O$) intermediate, and carboxylate (COO^-) species. While no significant correlation was found among of these intermediate species and by-product, the accurate catalytic mechanism was still unclear. Therefore, first-principle theoretical calculations were applied to explore the reaction mechanism and rate determining step.

3.6.2. *First-principle theoretical calculations*

Combined with *in situ* DRIFT results, detailed reaction pathways of acetone catalytic oxidation over catalyst surfaces were investigated by theoretical calculation method. The calculations were employed to study three issues: (1) the activation of oxygen molecules, (2) the activation of acetone molecules, and (3) the formation of intermediate species and byproduct. The Mn_3O_4 (001) surface was the most acceptable model for investigating the catalytic oxidation of acetone.

(1) Adsorption energy and modes of acetone and O_2

The DFT adsorption energy and modes of the acetone and O_2 molecule on Mn_3O_4 (001) are shown in **Figure S4,** respectively. The adsorption energy of O_2 molecules adsorbed with $Mn_{(III)}Mn_{(II)}$ bond (-1.73 eV) and $Mn_{(III)}Mn_{(III)}$ bond (-1.15 eV) was much less than that of O_2 molecules adsorbed with one $Mn_{(II)}$ ion forming the peroxy-ring (-0.24 eV). Additionally, by comparing the DFT adsorption energy of

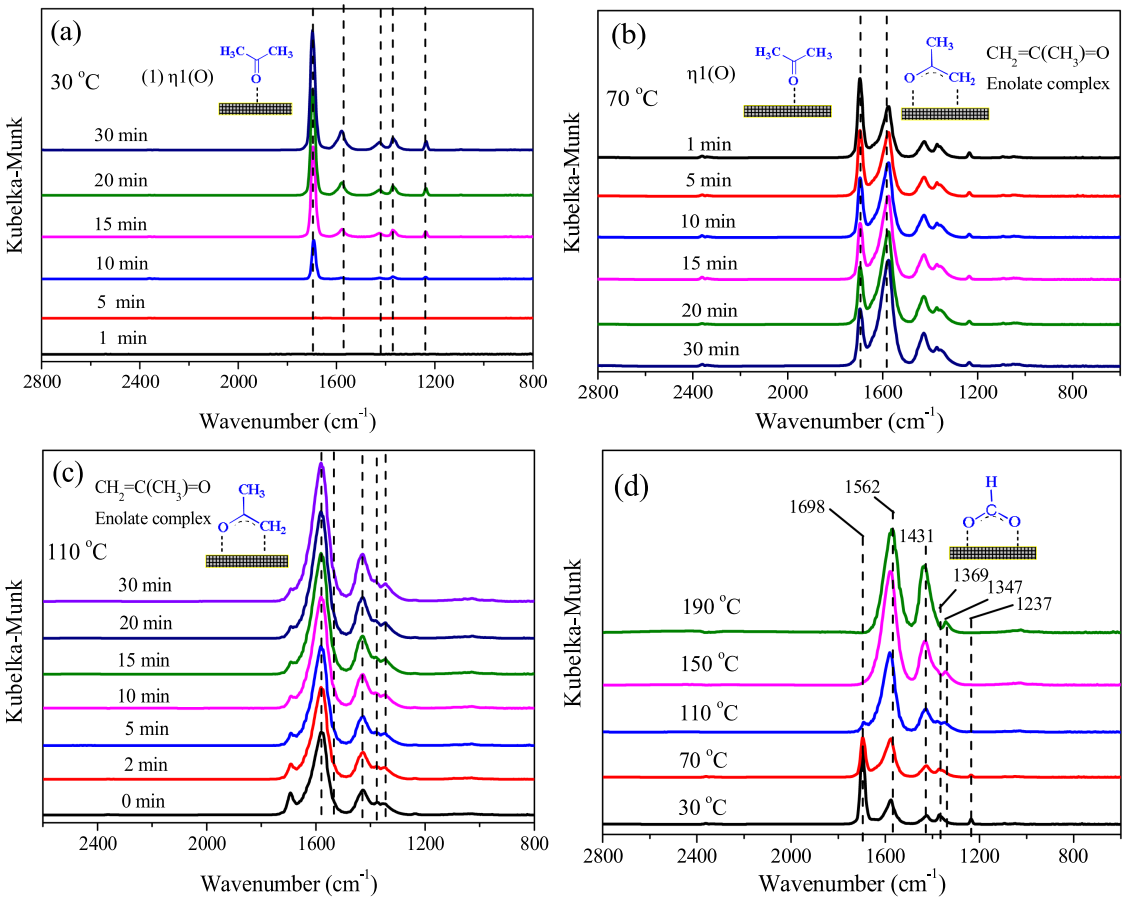

Fig. 7. *In situ* DRIFT spectra of acetone catalytic oxidation for Mn_3AlO catalyst at different reaction times and temperatures.

the acetone molecule, the O_2 molecules were preferably adsorbed on the Mn_3O_4 (001) surface since the adsorption energy of O_2 was much less than that of acetone molecule (-0.36 eV and -0.53 eV on $Mn_{(III)}$ and $Mn_{(II)}$ top site). A detailed schematic diagram as shown in follows:

The adsorption of O_2 molecules:

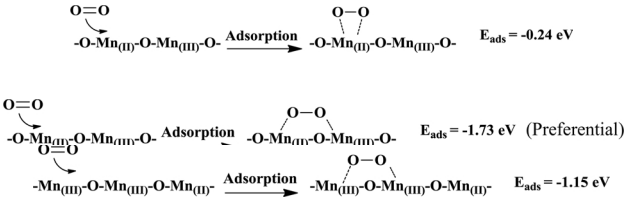

The adsorption of acetone molecules:

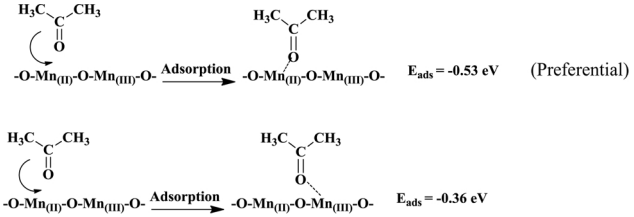

(2) O_2 dissociation

The energy pathways for O_2 dissociation on the Mn_3O_4 (001) surface was analyzed, as shown in **Figure S5**. The activation energies for the O_2 decomposition were 0.66 eV and 0.63 eV for the $Mn_{(III)}Mn_{(II)}$ and $Mn_{(III)}Mn_{(III)}$ bonds, respectively. When O_2 adsorbed with one $Mn_{(II)}$ ion forming the peroxy-ring, its dissociation barrier was much greater (0.72 eV) than the two formers. Therefore, O_2 was preferred to dissociate and then participate in the reaction. A detailed schematic diagram as shown in follows:

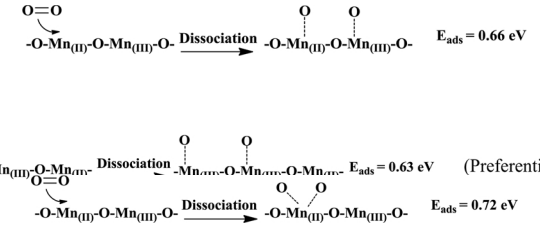

(3) The activation of acetone molecules and intermediate species

According to the intermediate species obtained from *in situ* DRIFT spectra, the detailed reaction pathways were analyzed from three stages:

- α-H abstraction of the acetone molecule

According to the frontier orbital theory, the carbonyl group of acetone showed a tendency to bond with the Mn terminals, in accordance with *in situ* DRIFT spectra results. After the acetone molecules adsorbed on the catalysts surface (η1(O) adsorption species), the initial step of dehydrogenation was the formation of $CH_2(CH_3)CO^*$ (0.48 eV). This intermediate species was also detected by *in situ* DRIFT spectra and the schematic diagram is shown as follows:

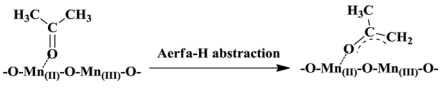

- C–C bond breaking steps

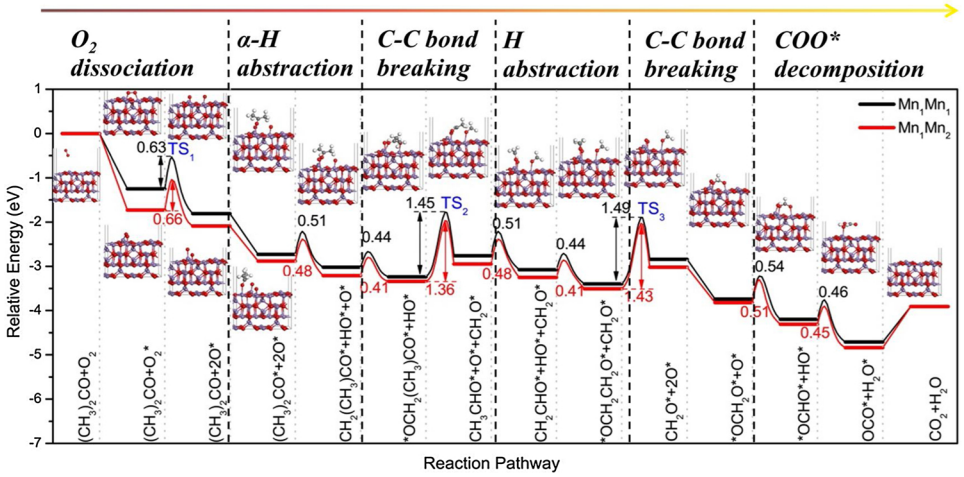

Fig. 8. Reaction pathways for the acetone catalytic oxidation on the Mn_3O_4 surface. Values for activation and reaction energies (eV) are given with respect to the energy of the reactants into each step.

When the $CH_2(CH_3)CO^*$ (0.48 eV) intermediate species was formed, which is followed by the breaking of C—C bonds to produce the CH_3CHO^* species (1.36 eV) that is further dissociated and/or desorbed to form CH_2O^* and/or $CH_3CHO_{(gas)}$, $CH_3CHO_{(gas)}$ byproduct was also detected. Therefore, the actual situation C—C bond breaking steps was further verified. A detailed schematic diagram is shown as follows:

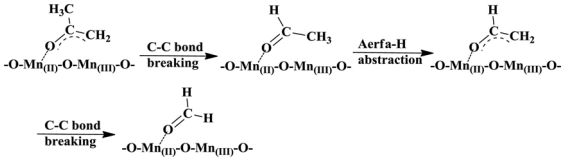

- CH_2O^* decomposition

Finally, the CH_2O^* group (0.54 eV) attacked by dissociated oxygen (O*) and further dehydrogenation occurred, yielding H_2O and CO_2 via the COO^- adsorbed species (0.46 eV). The intermediate species were also proved by *in situ* DRIFT spectra and the reaction process as follows.

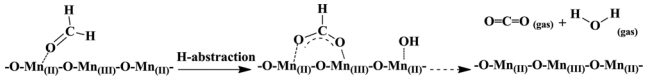

Combined with *in situ* DRIFT and first-principle calculations, detailed reaction pathways of acetone catalytic oxidation over the catalyst surface were investigated and shown in Fig. 8. The following major steps were performed: O_2 dissociated into oxygen atoms, acetone decomposed into CH_2O^* via α-H abstraction and C—C bond breaking process, and CH_2O^* further decomposed into CO_2 and H_2O, where * stands for an adsorption atom of the intermediates. The surface Mn atoms acted as the active sites for the formation of atomic oxygen and activation of acetone molecules, the high energy barrier of C—C bond breaking was mainly the rate determining step in acetone oxidation.

4. Conclusions

In this study, surface properties enhanced Mn_xAlO oxide catalysts were synthesized and applied to explore the catalytic performance and reaction mechanism. The surface intrinsic and/or formative oxygen vacancy can induce the Mn-O bond of structural unit [MnO_6] weakened, and then enhance the redox properties of catalysts, O_2 molecule dissociation and reactive oxygen species produced. Consequently, the remarkable catalytic activity, stability and water-resistance properties of Mn_3AlO catalysts were displayed. Besidies, *in situ* DRIFT technique and theoretical calculations was used to study the reaction mechanism. The main intermediate species and/or transient state, including $\eta1(O)_{(ads)}$, $CH_2=C(CH_3)=O_{(ads)}$, O*, CH_3CHO^*, CH_2O^* and $COO_{(ads)}$, was captured and predicted during the reaction progress. The main reaction steps were tentatively elaborated as follows: α-H abstraction, O_2 molecule dissociation, and C—C bond breaking. Particularly, the C—C bond breaking was the main limited step for acetone oxidation. Hence, the proposed catalysts may provide an excellent project for a wide range of environmental protection applications.

Acknowledgements

This work is financially supported by the National Key R&D Program of China (2016YFC0204203), National Natural Science Foundation of China (21337003, 21707152), and Beijing Municipal Science & Technology Commission (Z181100000118003). We also thank Dr. Huan Duan (Southwest University) for him support while performing first-principle theoretical calculations.

Appendix A. Supplementary data

Supplementary material related to this article can be found, in the online version, at doi:https://doi.org/10.1016/j.apcatb.2019.03.035.

References

[1] H.B. Singh, M. Kanakidou, P.J. Crutzen, D.J. Jacob, High concentrations and photochemical fate of oxygenated hydrocarbons in the global troposphere, Nature 378 (1995) 50–54.
[2] A. Kumar, C.P. Alaimo, R. Horowitz, F.M. Mitloehner, M.J. Kleeman, P.G. Green, Volatile organic compound emissions from green waste composting: characterization and ozone formation, Atmos. Environ. 45 (2011) 1841–1848.
[3] R. Seco, J. Peñuelas, I. Filella, Short-chain oxygenated VOCs: emission and uptake by plants and atmospheric sources, sinks, and concentrations, Atmos. Environ. 41 (2007) 2477–2499.
[4] T. Wu, X. Wang, Emission of oxygenated volatile organic compounds (OVOCs) during the aerobic decomposition of orange wastes, J. Environ. Sci. 33 (2015) 69–77.
[5] A. Mellouki, T.J. Wallington, J. Chen, Atmospheric chemistry of oxygenated volatile organic compounds: impacts on air quality and climate, Chem. Rev. 115 (2015) 3984–4014.
[6] M.S. Kamal, S.A. Razzak, M.M. Hossain, Catalytic oxidation of volatile organic compounds (VOCs)–a review, Atmos. Environ. 140 (2016) 117–134.
[7] C. Hu, Q. Zhu, Z. Jiang, L. Chen, R. Wu, Catalytic combustion of dilute acetone over Cu-doped ceria catalysts, Chem. Eng. J. 152 (2009) 583–590.
[8] N. Rezlescu, E. Rezlescu, P.D. Popa, C. Doroftei, M. Ignat, Partial substitution of manganese with cerium in $SrMnO_3$ nano-perovskite catalyst. Effect of the modification on the catalytic combustion of dilute acetone, Mater. Chem. Phys. 182 (2016) 332–337.

[9] V. Blasin-Aubé, J. Belkouch, L. Monceaux, General study of catalytic oxidation of various VOCs over $La_{0.8}Sr_{0.2}MnO_{3+x}$ perovskite catalyst-influence of mixture, Appl. Catal. B Environ. 43 (2003) 175–186.
[10] R. Spinicci, M. Faticanti, P. Marini, S. De Rossi, P. Porta, Catalytic activity of $LaMnO_3$ and $LaCoO_3$ perovskites towards VOCs combustion, J. Mol. Catal. A Chem. 197 (2003) 147–155.
[11] C. Hu, Enhanced catalytic activity and stability of $Cu_{0.13}Ce_{0.87}O_y$ catalyst for acetone combustion: effect of calcination temperature, Chem. Eng. J. 159 (2010) 129–137.
[12] L.Y. Lin, C. Wang, H. Bai, A comparative investigation on the low-temperature catalytic oxidation of acetone over porous aluminosilicate-supported cerium oxides, Chem. Eng. J. 264 (2015) 835–844.
[13] L.Y. Lin, H. Bai, Salt-templated synthesis of Ce/Al catalysts supported on mesoporous silica for acetone oxidation, Appl. Catal. B Environ. 148–149 (2014) 366–376.
[14] Q. Wang, D. O'Hare, Recent advances in the synthesis and application of layered double hydroxide (LDH) nanosheets, Chem. Rev. 112 (2012) 4124–4155.
[15] F. Zhang, X. Zhang, Z. Hao, G. Jiang, H. Yang, S. Qu, Insight into the H_2S selective catalytic oxidation performance on well-mixed Ce-containing rare earth catalysts derived from MgAlCe layered double hydroxides, J. Hazard. Mater. 342 (2018) 749–757.
[16] Y. Wang, D. Yan, S. El Hankari, Y. Zou, S. Wang, Recent progress on layered double hydroxides and their derivatives for electrocatalytic water splitting, Adv. Sci. 5 (2018) 1800064.
[17] H. Huang, Y. Xu, Q. Feng, D.Y.C. Leung, Low temperature catalytic oxidation of volatile organic compounds: a review, Catal. Sci. Technol. 5 (2015) 2649–2669.
[18] Z. Hou, J. Feng, T. Lin, H. Zhang, X. Zhou, Y. Chen, The performance of manganese-based catalysts with $Ce_{0.65}Zr_{0.35}O_2$ as support for catalytic oxidation of toluene, Appl. Surf. Sci. 434 (2018) 82–90.
[19] Z. Ye, J.M. Giraudon, N. Nuns, P. Simon, N. De Geyter, R. Morent, J.F. Lamonier, Influence of the preparation method on the activity of copper-manganese oxides for toluene total oxidation, Appl. Catal. B Environ. 223 (2018) 154–166.
[20] B. Faure, P. Alphonse, Co-Mn-oxide spinel catalysts for CO and propane oxidation at mild temperature, Appl. Catal. B Environ. 180 (2016) 715–725.
[21] X. Wang, Y. Liu, Y. Zhang, T. Zhang, H. Chang, Y. Zhang, L. Jiang, Structural requirements of manganese oxides for methane oxidation: XAS spectroscopy and transition-state studies, Appl. Catal. B Environ. 229 (2018) 52–62.
[22] H. Xu, N. Yan, Z. Qu, W. Liu, J. Mei, W. Huang, S. Zhao, Gaseous heterogeneous catalytic reactions over Mn-based oxides for environmental applications: a critical review, Environ. Sci. Technol. 51 (2017) 8879–8892.
[23] Y. Sun, N. Li, X. Xing, X. Zhang, Z. Zhang, G. Wang, J. Cheng, Z. Hao, Catalytic oxidation performances of typical oxygenated volatile organic compounds (acetone and acetaldehyde) over MAlO (M = Mn, Co, Ni, Fe) hydrotalcite-derived oxides, Catal. Today 327 (2019) 389–397.
[24] J. Huang, S. Zhong, Y. Dai, C.C. Liu, H. Zhang, Effect of MnO_2 phase structure on the oxidative reactivity toward bisphenol a degradation, Environ. Sci. Technol. 52 (2018) 11309–11318.
[25] V. Blum, R. Gehrke, F. Hanke, P. Havu, V. Havu, X. Ren, K. Reuter, M. Scheffler, Ab initio molecular simulations with numeric atom-centered orbitals, Comput. Phys. Commun. 180 (2009) 2175–2196.
[26] J.P. Perdew, K. Burke, M. Ernzerhof, Generalized gradient approximation made simple, Phys. Rev. Lett. 77 (1996) 3865–3868.
[27] H.J. Monkhorst, J.D. Pack, Special points for brillouin-zone integrations, Phys. Rev. B 13 (1976) 5188–5192.
[28] A. Tkatchenko, M. Scheffler, Accurate molecular van der waals interactions from ground-state electron density and free-atom reference data, Phys. Rev. Lett. 102 (2009) 073005.
[29] G. Henkelman, H. Jónsson, Improved tangent estimate in the nudged elastic band method for finding minimum energy paths and saddle points, J. Chem. Phys. 113 (2000) 9978–9985.
[30] S. Rong, K. Li, P. Zhang, F. Liu, J. Zhang, Potassium associated manganese vacancy in birnessite-type manganese dioxide for airborne formaldehyde oxidation, Catal. Sci. Technol. 8 (2018) 1799–1812.
[31] B. Bai, J. Li, J. Hao, 1D-MnO_2, 2D-MnO_2 and 3D-MnO_2 for low-temperature oxidation of ethanol, Appl. Catal. B Environ. 164 (2015) 241–250.
[32] Y. Luo, Y. Zheng, J. Zuo, X. Feng, X. Wang, T. Zhang, K. Zhang, L. Jiang, Insights into the high performance of Mn-Co oxides derived from metal-organic frameworks for total toluene oxidation, J. Hazard. Mater. 349 (2018) 119–127.
[33] Y. Sun, J. Liu, J. Song, S. Huang, N. Yang, J. Zhang, Y. Sun, Y. Zhu, Exploring the effect of Co_3O_4 nanocatalysts with different dimensional architectures on methane combustion, ChemCatChem 8 (2016) 540–545.
[34] Y. Xie, Y. Yu, X. Gong, Y. Guo, Y. Guo, Y. Wang, G. Lu, Effect of the crystal plane figure on the catalytic performance of MnO_2 for the total oxidation of propane, CrystEngComm 17 (2015) 3005–3014.
[35] H. Pan, Y. Jian, C. Chen, C. He, Z. Hao, Z. Shen, H. Liu, Sphere-shaped Mn_3O_4 catalyst with remarkable low-temperature activity for methyl-ethyl-ketone combustion, Environ. Sci. Technol. 51 (2017) 6288–6297.
[36] C. He, Y. Yu, C. Chen, L. Yue, N. Qiao, Q. Shen, J. Chen, Z. Hao, Facile preparation of 3D ordered mesoporous CuO_x-CeO_2 with notably enhanced efficiency for the low temperature oxidation of heteroatom-containing volatile organic compounds, RSC Adv. 3 (2013) 19639–19656.
[37] Y.J. Wei, L.Y. Yan, C.Z. Wang, X.G. Xu, F. Wu, G. Chen, Effects of Ni doping on $[MnO_6]$ octahedron in $LiMn_2O_4$, J. Phys. Chem. B 108 (2004) 18547–18551.
[38] B.D. Napruszewska, A. Michalik-Zym, R. Dula, E. Bielańska, W. Rojek, T. Machej, R.P. Socha, L. Lityńska-Dobrzyńska, K. Bahranowski, E.M. Serwicka, Composites derived from exfoliated laponite and Mn-Al hydrotalcite prepared in inverse microemulsion: a new strategy for design of robust VOCs combustion catalysts, Appl. Catal. B Environ. 211 (2017) 46–56.
[39] F. Wang, H. Dai, J. Deng, G. Bai, K. Ji, Y. Liu, Manganese oxides with rod-, wire-, tube-, and flower-like morphologies: highly effective catalysts for the removal of toluene, Environ. Sci. Technol. 46 (2012) 4034–4041.
[40] P.R. Garcês Gonçalves, H.A. De Abreu, H.A. Duarte, Stability, structural, and electronic properties of hausmannite (Mn_3O_4) surfaces and their interaction with water, J. Phys. Chem. C 122 (2018) 20841–20849.
[41] R. King, H. Idriss, Acetone reactions over the surfaces of polycrystalline UO_2: a kinetic and spectroscopic study, Langmuir 25 (2009) 4543–4555.
[42] M.D. Hernández-Alonso, I. Tejedor-Tejedor, J.M. Coronado, M.A. Anderson, J. Soria, Operando FTIR study of the photocatalytic oxidation of acetone in air over TiO_2-ZrO_2 thin films, Catal. Today 143 (2009) 364–373.
[43] H. Miyata, Y. Toda, Y. Kubokawa, Infrared studies of adsorption of acetone on MgO and NiO, J.Catal. (1974) 155–158.
[44] H. Miyata, M. Wakakmiya, M. Kubokawa, Infrared studies of interaction of oxygen with 2-propanol and acetone adsorbed on MgO and NiO, J. Catal. (1974) 117–123.